



Environmentally friendly $\text{YIn}_{0.9}\text{Fe}_{0.1}\text{O}_3$ -ZnO yellow pigment displaying near infra red (NIR) reflectance and photocatalytic activity

Michele Fedel^{a,*}, Andrea Rosati^a, Stefano Rossi^a, Marcello Picollo^b, Francesco Parrino^a

^a Department of Industrial Engineering, University of Trento, via Sommarive n. 9, 38123, Trento, Italy

^b Institute for Applied Physics “Nello Carrara” of the Italian National Research Council (IFAC-CNR), Via Madonna del Piano 10, 50019, Sesto Fiorentino, Italy

ARTICLE INFO

Handling editor: P. Vincenzini

Keywords:

Near infra red reflectance
Photocatalysis
Pigments
 $\text{YIn}_{0.9}\text{Fe}_{0.1}\text{O}_3$
Coatings

ABSTRACT

In this research, we produced ochre/yellow pigments of $\text{YIn}_{0.9}\text{Fe}_{0.1}\text{O}_3$, combined with ZnO pigments, through a citrate-assisted sol-gel approach. We investigated the impact of varying ZnO addition methods (incorporated into the sol-gel bath and physically mixed with $\text{YIn}_{0.9}\text{Fe}_{0.1}\text{O}_3$ pigments) on their color properties, near-infrared (NIR) reflectance and photocatalytic activity. The effect of the different ZnO addition methods was investigated on precursors and final calcined pigments through X-ray diffraction (XRD), Vis-NIR reflectance, Fourier transform infrared spectroscopy (FT-IR) Scanning Electron Microscope (SEM) and thermal analyses such as thermogravimetry (TGA), and differential scanning calorimetry (DSC). The synthesized nanocomposites were evaluated for their photocatalytic characteristics by examining the degradation of 4-Nitrophenol (4-NP) when exposed to UV radiation. The potential environmental applications of the pigments were investigated not only for direct pollutant degradation but also in terms of energetic sustainability. In fact, the developed pigments can be employed as passive cooling materials to mitigate the temperature of buildings, thus dramatically reducing energy consumption. For this reason, the pigments were embedded into a polymeric binder and coated onto roofing aluminum sheets. The obtained coatings were investigated in terms of NIR reflectance and heat adsorption. The photocatalytic ability of the coatings was assessed by the degradation of 4-NP and methylene blue (MB) under xenon arc lamp. The results obtained indicate the feasibility of producing a pale yellow pigment with both NIR reflectance and photocatalytic capabilities.

1. Introduction

Infrastructure development in urban environments caused the gradual replacement of vegetation with heat-absorbing materials, such as bitumen, concrete, and limes. Those materials absorb and store solar radiation and affect the exchange of moisture between the soil and the atmosphere, known as evapotranspiration, which impacts the thermal conditions of urban areas. The heat-absorbing materials used in urban pavement and construction have been identified as contributors to a distinctive phenomenon known as the urban heat island (UHI) effect [1, 2]. Heat islands form due to the rise in surface temperatures and overall ambient temperatures experienced in urban areas in comparison with adjacent rural areas (naturally covered by trees and vegetation). The warming effect induced by paving and roofing materials contributes to the occurrence of heat waves, human discomfort, and heat-related illnesses. As a result, energy consumption surges in the summer months, driven by the extensive use of environmental comfort technologies,

including ventilation and air-conditioning (HVAC) systems within buildings. Indeed, HVAC technologies alone account for 40% of a building's total energy consumption [3]. In this scenario, passive cooling technologies serve as a means to mitigate the urban heat island effect and improve indoor thermal comfort in buildings without relying on energy consumption. Different passive cooling technologies, such as phase change materials (PCM) [4] and radiative materials designed for application on roofs, facades, and pavement surfaces [5], were investigated to mitigate the temperature of the buildings in urban settlements. Out of the examined technological solutions, NIR reflective pigments emerge as a promising strategy for effectively mitigating Urban Heat Island (UHI) effects. Considering the whole solar radiation spectrum, the near-infrared portion (NIR, 700–2500 nm) [6] is the major component (52%).

The remaining portion consists of 5% ultraviolet radiation (UV, 300–400 nm) and 43% visible light (VIS, 400–700 nm). In the last decade, various initiatives have been pursued to develop near-infrared

* Corresponding author.

E-mail address: michele.fedel@unitn.it (M. Fedel).

<https://doi.org/10.1016/j.ceramint.2024.02.075>

Received 27 December 2023; Received in revised form 2 February 2024; Accepted 6 February 2024

Available online 12 February 2024

0272-8842/© 2024 The Authors. Published by Elsevier Ltd. This is an open access article under the CC BY-NC-ND license (<http://creativecommons.org/licenses/by-nc-nd/4.0/>).

(NIR) reflective pigments designed for incorporation into cool coatings. These pigments effectively reflect NIR radiation, contributing to a substantial reduction in absorbed heat. According to the literature, highly reflective materials such as ZnO, Fe₂O₃, TiO₂ (anatase and rutile phases), Al₂O₃, are often employed in synthesizing NIR reflective materials [7–9]. Specifically, numerous studies have unveiled the influence of different crystalline phases on the chemical and optical properties of the synthesized pigments. This encompasses factors such as color characteristics and near-infrared (NIR) reflectance. Sadeghi-Niaraki et al. [10] have increased NIR reflectance of Fe₂O₃ by applying a thin layer of TiO₂, while Jose et al. [11] discovered that the addition of ZnO to YIn_{0.9}Mn_{0.1}O₃ using a sol-gel route led to an increase in NIR solar reflectance from 50% to 70%.

Apart from overheating buildings, urban areas contend with pollution generated and emitted primarily through combustion processes in densely populated urban environments. In this context, photocatalytic degradation for pollutant removal has revealed an attractive solution to increase local air quality. Photocatalytic processes facilitate the mineralization of hazardous compounds under gentle conditions by harnessing the generation of electron-hole pairs induced by light, which initiates the formation of highly reactive radical species [12]. Given that specific materials display both photocatalytic and reflective characteristics, it becomes possible to formulate composite compounds that can achieve both near-infrared (NIR) reflection and simultaneously facilitate photocatalytic air purification. As previously mentioned, enhancing near-infrared (NIR) reflectance capability depends on combining distinct crystalline phases with specific characteristics, and a similar approach is applicable in the field of photocatalysis [13–15]. In fact, ZnO and Fe₂O₃ find applications both as photocatalytic and NIR reflective materials [13,16] as well as TiO₂ [10,16]. In the case of Fe₂O₃, it has been observed that when coupled with TiO₂ or ZnO, the absorption range of the material towards visible light is extended, and its photocatalytic activity enhanced [13,17]. In fact, coupling different semiconductors of suitable electronic properties leads to spatial separation of the photogenerated charges with a consequent reduction of their recombination. Therefore, synergistic systems typically exhibit a higher level of photocatalytic activity compared to what is observed in the presence of individual components [10,18].

The YIn_{1-x}Fe_xO₃ stoichiometry produces colourful pigments with average NIR radiation efficiency [11,19]. Solid solutions based on YFeO₃ [20] are promising photocatalyst [20–23], but only limited literature regarding NIR reflectance of YFeO₃ based materials is available [24,25]. YIn_{1-x}Fe_xO₃ and YFeO₃-based pigments seem to be a promising solution to combine NIR reflectance and photocatalytic activity, considering that environmentally friendly production routes (such as the precipitation [24], the sol-gel methods [26] and solid state reaction [27]) can be employed. The sol-gel synthesis route employs low calcination temperatures for a limited time, does not use toxic materials, and limits residual wastes [19,28]. The YIn_{1-x}Fe_xO₃-based pigments exhibit a yellow, ochre-red hue, making them a potential alternative to traditional yellow pigments based on toxic chrome yellow (PbCrO₄) or solid solutions of Pb(Cr,S)O₄. The pigments based on Cr and Pb, extensively utilized in road and traffic paints, are now being acknowledged as contributors to lead and hexavalent chromium contamination in water and sediments [29,30].

In this research, we developed doped YInO₃ pigments containing Fe to produce an ochre/yellow pigment possessing both NIR reflectance properties and photocatalytic activity. The effect of adding ZnO nanoparticles to the NIR reflectance was also investigated. Specifically, YIn_{0.9}Fe_{0.1}O₃ pigments were synthesized using the citrate-assisted sol-gel method, with and without the addition of ZnO nanopowders (ZnO <100 nm). Moreover, ZnO was introduced directly during the synthesis, following previously reported synthesis routes [11,31], or it was mechanically mixed with the synthesized YIn_{0.9}Fe_{0.1}O₃ pigment after the completion of the synthesis. We have examined the impact of distinct ZnO addition methods on the materials' physico-chemical and

appearance properties. Additionally, we have assessed the NIR reflective properties and the photocatalytic activity of the developed pigments. Finally, the pigments were dispersed in a commercial acrylic binder and deposited on aluminum roofing sheets to test the photocatalytic activity and NIR reflectance. The developed pigments demonstrated their potential both as passive cooling materials to mitigate the temperature of buildings (thus enabling dramatic reduction of building energetic consumption) and as a support for direct photocatalytic degradation of atmospheric pollutants.

2. Materials and methods

2.1. Materials

Y₂O₃ (99.99%, Sigma-Aldrich), In₂O₃ (99.99%, Sigma-Aldrich), FeCl₂•4H₂O (>99%, Sigma-Aldrich), ZnO nanopowders with a particle size of <100 nm (approximately 80% Zn, Sigma-Aldrich), and citric acid (99%, Sigma-Aldrich) were utilized without any additional purification. Sol-gel synthesis of YIn_{0.9}Fe_{0.1}O₃ pigments (Fig. 1a) was performed according to a procedure described in a previous work [31]. Briefly, to ensure a comprehensive overview, we recall here the synthesis route. Stoichiometric amounts of yttrium oxide (1.66 mmol), iron (II) chloride tetrahydrate (0.33 mmol), and indium oxide (1.49 mmol) were dissolved in 4.0 M nitric acid (100 mL) under constant stirring at 800 rpm, maintaining a temperature of 50 °C. After 1 h, a homogenous solution was obtained. Citric acid was then introduced in a stoichiometric proportion with a molar ratio of 3.5:1 relative to the metal cations. After 6 h of continuous stirring, the resultant yellow solution underwent drying at 80 °C until a dried gel was formed. Subsequently, the gel was heated to 250 °C to induce nitrate decomposition, followed by calcination at 850 °C for 2 h. This process employed a heating rate of 5 °C/min in a high-temperature electric furnace (MAB). The identical procedure was duplicated for the synthesis of YInFeO - ZnO powders, illustrated in Fig. 1b. The only deviation was the inclusion of zinc oxide (3.33 mmol), which was dissolved in the 4.0 M nitric acid solution during the synthesis. The same procedure was replicated for the preparation of YInFeO - ZnO powders (as shown in), with the exception that zinc oxide (3.33 mmol) was dissolved in the 4.0 M nitric acid solution during the synthesis process.

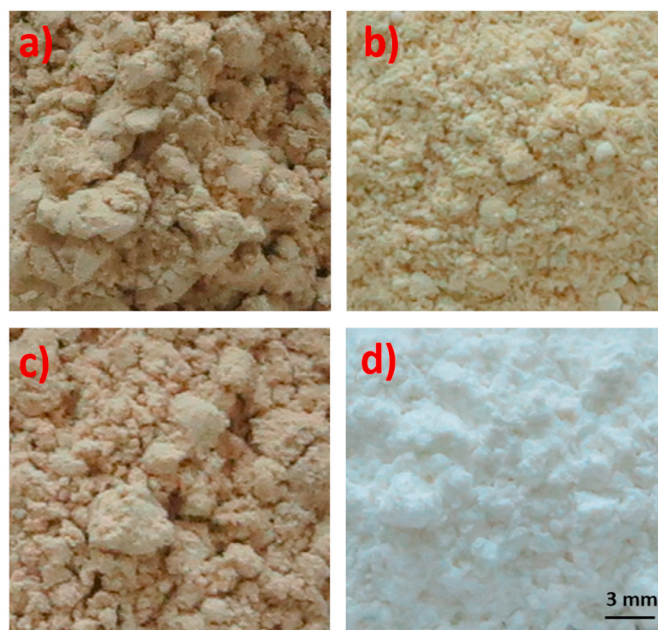


Fig. 1. Appearance of the investigated pigments: YInFeO (a), YInFeO - ZnO (b), YInFeO MIX ZnO (c), commercial ZnO (d).

In the case of the pigment obtained by mixing ZnO nanopowders (Fig. 1d) with $\text{YIn}_{0.9}\text{Fe}_{0.1}\text{O}_3$ (YInFeO MIX ZnO, Fig. 1c) the two components were mechanically mixed in an agate mortar (27 wt% of ZnO, bal. YInFeO). Table 1 presents an overview of the powders investigated in this study, including the diverse techniques utilized for their production, accompanied by their corresponding labels. Fig. 1 illustrates that the inclusion of ZnO leads to a lighter hue of the powder.

The photocatalytic behaviour of the synthesized pigments was investigated by using 4-Nitrophenol (4-NP) as a model pollutant. The degradation tests were carried out within a pyrex cylindrical photo-reactor ($V = 20$ ml), housing an aqueous suspension of 4-NP at a concentration of 0.3 mM. To this, varying quantities of pigments were introduced: 1 g/L of YInFeO, 0.5 g/L of ZnO, 1.85 g/L of YInFeO – ZnO and of YInFeO MIX ZnO. The suspension was kept at around 27 °C and stirred in darkness for 30 min to establish adsorption/desorption equilibrium. Following this, the suspension was subjected to irradiation by six UV actinic fluorescent lamps (each 14 W, Philips, primary emission at 365 nm, irradiance: 7 W/m^2), arranged in a hexagonal configuration around the reactor. Sampling from the solution was performed at specified time intervals. The solution samples were filtered through a 0.2 μm filter (HA, Millipore), acidified with predetermined amounts of concentrated H_2SO_4 , and subsequently analyzed using a UV–vis spectrophotometer (Shimadzu UV-1900i), with absorbance measured at 316 nm.

4 wt% of each pigment was dispersed in an acrylic binder consisting of a water-based clearcoat (Alpina, Daw Italia GmbH, Italy).

Prior to the deposition process, the mixture underwent ultrasonication (Hielscher ultrasound technology UP400S) for 60 min at 70% amplitude in a one-cycle mode, ensuring thorough mixing of the resulting solution (60 mL). 90 mm × 150 mm × 3 mm AA5005 (containing 0.7% Fe, 0.3% Si, 0.5% Mg, 0.25% Zn, 0.2% Mn, 0.2% Cu, 0.1% Cr, with aluminum as the balance) panels were employed as the substrate to coat. The panels underwent a pre-treatment process to enhance its adhesion to the organic coating. Specifically, it was subjected to a 6-min ultrasonic cleaning with ethanol, followed by etching in a room-temperature alkaline solution (5 wt% NaOH) for 120 s. Subsequently, it was pickled in a 34 v/v% HNO_3 solution for 60 s at room temperature. After each treatment, the panels were thoroughly washed with demineralized water.

The application of the paint onto the AA5005 plates was carried out using an Elcometer 4340 Motorized Film Applicator, to obtain a dry film coating thickness of approximately 100 μm . Four distinct coatings were prepared, as depicted in Fig. 2a. Additionally, we prepared a white reflective coating containing titanium (IV) oxide (Sigma-Aldrich 99.7%) and a black absorber coating containing graphite (Sigma-Aldrich 99.0% carbon basis) to serve as the positive and negative control, respectively (see Fig. 2b). Both titanium (IV) oxide and graphite were incorporated into the binder at the same concentration (4 wt%). Titanium (IV) oxide, specifically in the anatase form, was selected due to the extensive utilization in outdoor architectural applications, such as photocatalytic self-cleaning and high solar reflectance [32–34], and its commercial availability [32]. Graphite, employed as the negative control, finds extensive use in the fabrication of components known for their outstanding heat absorption properties [35] and in coatings designed for solar energy concentration [36]. Furthermore, experimental tests were carried out on the uncoated AA5005 aluminum sheet for comparative purposes. AA5005 aluminum sheets coated with acrylic binder and TiO_2

Table 1
Labelling and brief description of the preparation of the pigments.

Pigments label	Description
YInFeO	Sol-Gel derived $\text{YIn}_{0.9}\text{Fe}_{0.1}\text{O}_3$
YInFeO - ZnO	Sol-Gel derived $\text{YIn}_{0.9}\text{Fe}_{0.1}\text{O}_3$ with ZnO added during synthesis
YInFeO MIX ZnO	Sol-Gel derived $\text{YIn}_{0.9}\text{Fe}_{0.1}\text{O}_3$ mechanically mixed with ZnO
ZnO	ZnO, as supplied

were utilized as reference samples in photocatalytic tests. The labels reported in Table 2 were consistently utilized in the manuscript to reference the coatings within the text.

The photocatalytic activity of the coated samples was examined using both 4-NP and methylene blue (MB) as the model compounds. Square samples measuring 4 mm^2 (cut from the Qpanels) were immersed in a 20 mL stirred solution of the selected model compound with a concentration of 0.06 mM. Subsequently, they were irradiated using the xenon arc lamp employed for assessing thermal performances. The lamps were positioned 300 mm away from the solution, and samples collected at predefined time intervals were analyzed using UV–vis spectroscopy (Shimadzu UV-1900i), as described earlier.

2.2. Methods

Thermogravimetry (TGA) and differential scanning calorimetry (DSC) analyses were performed on the $\text{YIn}_{0.9}\text{Fe}_{0.1}\text{O}_3$ -ZnO dried gel to investigate the thermal decomposition processes (TGA) and the phase transitions (DSC). These analyses were conducted under ambient air conditions with a flow rate of 50 mL/min, covering the 50–1000 °C temperature range at a heating rate of 20 °C/min. A differential thermal analyser TG/DSC NETZSCH STA 409 PC Luxx was employed for this purpose. Additionally, Fourier transform infrared (FT-IR) spectra were acquired using a Varian 4100 FT-IR Excalibur Series instrument. The different powders, combined with spectroscopically pure KBr, were pressed into tablets to collect transmission spectra. The morphology and the particle size of the synthesized pigments were examined through low-vacuum scanning electron microscopy (SEM) utilizing a JEOL JSM-IT300 instrument equipped with an energy dispersive spectrometer (EDXS). The crystal structure of the pigments was investigated through X-ray diffraction (XRD) using an Italtstructures IPD3000 diffractometer. This instrument was equipped with a Co anode source, which featured a line focus. To minimize k-beta radiation, a multilayer monochromator was employed, along with fixed 100 μm slits. The XRD investigation was performed in the reflection geometry, maintaining a constant omega angle of 5° relative to the incident beam. Diffraction patterns were captured using an Inel CPS120 detector, covering the 5–120° 2 θ range, with a resolution of 0.03° per channel. All XRD measurements were conducted at room temperature and the refinement of the X-ray diffraction data was carried out using a JAVA-based software called Materials Analysis Using Diffraction (MAUD) [37,38]. The optical properties of the powdered pigments were evaluated using a PerkinElmer Lambda 1050 UV/VIS/NIR Spectrophotometer equipped with a 60 mm diameter integrating sphere. ZnO (99.0% purity) was used as a reference material. An equal quantity of each pigment (3 g) was measured, and the powders were placed in quartz cuvettes with standardized dimensions (5 mm × 20 mm × 30 mm) to ensure consistent measurements and mitigate any potential impact of particle distribution and material thickness. Reflectance spectra were recorded using a diffuse reflectance setup with a 0°/d geometry. The NIR solar reflectance (R^*) of the pigments was calculated using the following formula:

$$R^* = \frac{\int_{700}^{2500} r(\lambda)i(\lambda)d\lambda}{\int_{700}^{2500} i(\lambda)d\lambda}$$

here, $r(\lambda)$ represents the experimentally measured spectral reflectance (W/m^2) and $i(\lambda)$ stands for the solar spectral irradiance ($\text{W}\cdot\text{m}^{-2}\cdot\text{nm}^{-1}$), determined in accordance with the ASTM G173-03 guidelines [39]. Furthermore, the reflected power for each wavelength can be determined by multiplying the spectral irradiance data from ASTM G173-03 by the corresponding spectral paint reflectance.

The L^* , a^* , b^* color coordinates of the pigments and their corresponding visible reflectance spectra were ascertained using the CM-2600d Spectrophotometer, in conjunction with the analytical software Spectra Magic NX. The spectrophotometer was calibrated using a white standard. The data were collected at 10 nm intervals across the 360–740

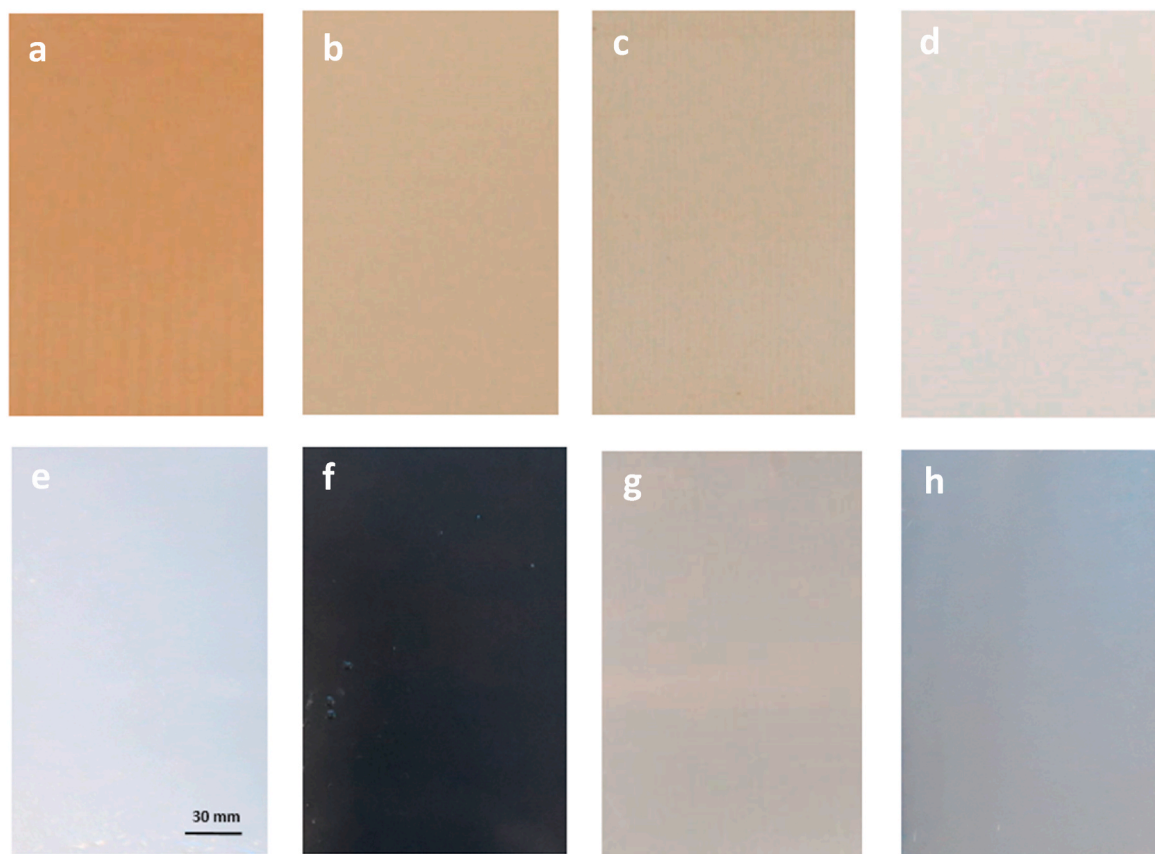


Fig. 2. Appearance of the AA5005 coated samples: (a) YInFeO + binder, (b) YInFeO-ZnO + binder, (c) YInFeO-MIX-ZnO + binder, (d) ZnO + binder (e) TiO₂ + binder, (f) Graphite + binder, (g) Binder, (h) Substrate.

Table 2

Summary of the coatings investigated in this study.

Labels	Polymeric binder	Pigments	
		Content	Nature
YInFeO + binder	Acrylic	4 wt%	YIn _{0.9} Fe _{0.1} O ₃
YInFeO-ZnO + binder			YIn _{0.9} Fe _{0.1} O ₃ -ZnO
YInFeO MIX ZnO + binder			YIn _{0.9} Fe _{0.1} O ₃ MIX
ZnO + binder			ZnO
TiO ₂ + binder			ZnO
Graphite + binder			TiO ₂
Binder			Graphite
Substrate	-	-	-

nm range. The colorimetric coordinates were determined based on the CIE-1976 Lab* color space [40], as recommended by the CIE (Commission Internationale de l'Eclairage). In this color space, L* represents the axis of lightness (ranging from black (0) to white (100)), a* denotes the axis of green (-) to red (+) axis, and b* represents the axis of blue (-) to yellow (+) axis.

Regarding the coatings, the same UV/VIS/NIR Spectrophotometer, CM-2600d Spectrophotometer, and SEM were employed to assess the optical and morphological properties.

The thermal performance of the coatings was assessed using the procedure previously described in [41]. The test specimens were positioned at a distance of 200 mm from the light source, which was a 1000 W Xenon arc lamp (Wissen). The investigated panels were positioned at the top of an open-topped box made from polyurethane foam sheets (dimensions: 150 mm × 270 mm × 200 mm). A thermocouple was positioned on the backside of the panel to obtain the temperature value (T_{panel}). The thermocouple was connected to a Delta OHM HD 32.7 RTD

data logging device to record the temperature values at 1-min intervals until a stable temperature plateau was achieved. The DeltaLog 9 software was used to manage the instrument. The temperature plateau value was considered as the parameter describing the overall thermal performance of the different coatings. All the measurements performed using the Xenon arc lamp were carried out in a controlled environment at about 25 °C.

3. Results and discussion

3.1. Pigments

Fig. 3a shows the TGA and DSC curves for the dried gel. The weight loss and the emergence of new phases were examined. The decomposition temperature, indicated by the highest rate of weight loss and represented by a descending peak, can be identified on the derivative curve (DTGA). The slight incline between 80 and 135 °C in the TGA curve corresponds to the elimination of adsorbed moisture. Upon closer examination using DTGA, the peak observed at 250 °C is associated with the decomposition of nitrates [42]. The peak observed at 400 °C was attributed to the decomposition of citric acid [42,43]. In the DSC curve (Fig. 3b), there are exothermic peaks observed at 250 °C and 400 °C, confirming the processes of nitrate and citrate decomposition, respectively. Additionally, the two closely positioned exothermic peaks at 420 °C and 450 °C are associated with citrate combustion [44]. Furthermore, the slight increase in heat flow observed between 600 °C and 850 °C can be attributed to the release of residual carbon-oxygen compounds [44]. Examining the DSC curve (Fig. 3b), an exothermic peak is observed within the temperature range of 700 °C–900 °C. This particular exothermic peak can be attributed to the formation of the crystalline phase of yttrium iron oxide [45]. Additionally, it is worth noting that

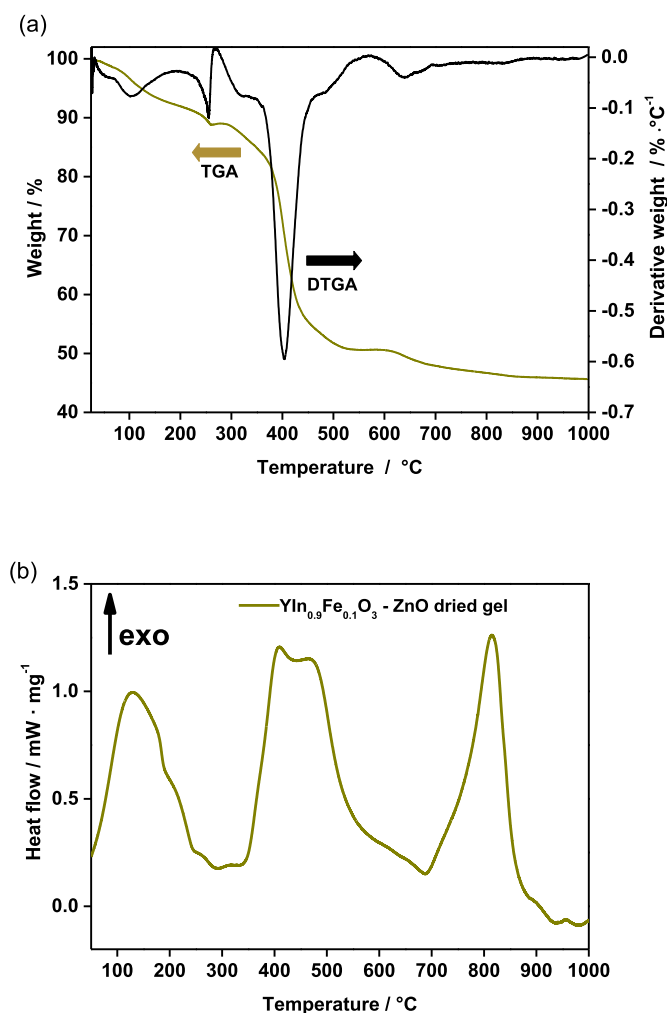


Fig. 3. TGA-DTGA (a) and DSC curves (b) of the YIn_{0.9}Fe_{0.1}O₃-ZnO dried gel.

nearly all of the organic components associated with the citrates undergo degradation beyond 650 °C.

Fig. S1 displays the FT-IR spectra of the synthesized pigments, revealing noteworthy features. The presence of the prominent band at 1384 cm⁻¹ was attributed to the nitrate stretching vibrations [46,47]. This suggests that non-degraded nitrates persist even at elevated temperatures, up to 850 °C. Other significant bands include those linked to the indium-oxygen bond (603 cm⁻¹) [46] and Y-O stretching vibrations [48–50] (568 cm⁻¹ and 497 cm⁻¹). In the FTIR spectra of YInFeO - ZnO and YInFeO MIX ZnO, the peaks corresponding to the asymmetric stretching vibration of Fe-O are present [27,51,52].

In the case of the ZnO pigment, the signal of wurtzite is observed at 464 cm⁻¹ [53]. Fig. 4 shows the appearance of the YInFeO - ZnO and YInFeO MIX ZnO powders. YInFeO - ZnO (Fig. 4a and b) are characterized by larger ZnO particles as apparent compared to YInFeO MIX ZnO (Fig. 4c and d). The latter exhibits a more homogeneous dispersion of ZnO, attributed to mechanical mixing, which facilitates an even distribution of ZnO nanoparticles within the mixture. Conversely, in the case of YInFeO - ZnO, nitric acid dissolves ZnO, leading to recrystallization and growth of larger ZnO particles through a coarsening mechanism, as observed in similar experimental conditions [54]. A visual comparison with the other synthesized pigments is provided in Fig. S2.

Fig. 5a displays the XRD patterns of the pigments under investigation along with their corresponding crystal structure (Fig. 5b). The Rietveld refinement process was conducted utilizing the MAUD software [37,38,55,56]. The quality of refinement was assessed based on the obtained weighted profile R factor (R_{wp}) and the idealized R_{wp} value known as the

expected R factor (R_{exp}), which served as refining quality parameters (see Table 3). The background was fitted using a third-order polynomial, and the cell value parameters for both the hexagonal and cubic phases of YIn_{0.9}Fe_{0.1}O₃ (JCPDS Card 70–0133 and JCPDS Card 25–1172, respectively), and ZnO (JCPDS Card 36–1451) were refined to enhance the overall fit. Because the JCPDS data files corresponding to the Y₂Fe₂O₇ pyrochlore structure are still not available on COD (Crystallography Open Database), the XRD pattern was obtained from [57] (file: mp-1568,804.cif). All synthesized pigments (YInFeO, YInFeO - ZnO, YInFeO MIX ZnO) show cubic and hexagonal phases of YIn_{0.9}Fe_{0.1}O₃ (Fig. 5b) while ZnO is present as a hexagonal phase. In contrast to similar systems like YIn_{0.9}Mn_{0.1}O₃, where the cubic-hexagonal transition concluded above 850 °C [31], the YIn_{0.9}Fe_{0.1}O₃ system exhibited the coexistence of cubic and hexagonal phases up to 850 °C. This behaviour is not unusual [58]. In previously studies concerning YInO₃, it has been reported that the cubic-hexagonal transformation initiates at 900 °C and completes around 1100 °C [58,59], or it commences at 1000 °C and concludes at 1250 °C [60] or even higher temperatures [61]. Additionally, Shukla et al. [58] observed a biphasic compound in the YIn_{1-x}Fe_xO₃ system for values of x ranging from 0.3 to 0.9. The presence of two phases in the compound arises from the transition of YInO₃ from an unstable cubic phase to a hexagonal phase. Increasing the temperature leads to a decrease in the cubic metastable phase and an increase in the hexagonal phase. The preservation of the cubic phase stability up to 850 °C is likely attributed to the disparity in size between the A-site (Y³⁺) and B-site (In_{1-x}Fe_x). The presence of In at a concentration of 0.9 brings about a convergence in relative ionic radii, aligning with the structural requirements of C-type structures.

According to the numerical values obtained with the Rietveld refinement (Table 3), the hexagonal phase in YInFeO pigment is about 5.65%. A low percentage of the hexagonal phase of YIn_{0.9}Fe_{0.1}O₃ is also present in YInFeO MIX ZnO (2.51 %). The hexagonal phase of YIn_{0.9}Fe_{0.1}O₃ is about 56.21% in YInFeO - ZnO. It appears that ZnO also serves as a favored site for the nucleation and growth of YIn_{0.9}Fe_{0.1}O₃ with a hexagonal phase. X-ray diffraction studies have confirmed the formation of epitaxial hexagonal phases over wurtzite ZnO core particles [62,63]. Those findings suggest that, in our case, the formation of a higher amount of hexagonal YIn_{0.9}Fe_{0.1}O₃ is not due only to thermal stability but is likely related to the presence of ZnO crystals. Thus, the pigments nucleate and grow on ZnO surface through the citrate sol-gel method [64].

The other crystalline phase observed in the pigments is Y₂Fe₂O₇ with a pyrochlore structure (Fig. 5b). A third phase formation was observed in the study of Shukla et al. [58], where an orthorhombic YFeO₃ garnet was obtained. In this study, we have found the Y₂Fe₂O₇ pyrochlore structure instead of YFeO₃ garnet. This is probably due to the different precursors employed in this study with respect to Shukla et al. [58], which reflects in the atomic recombination. A similar structure, Y₃Fe₅O₁₂ garnet, was also obtained via-citrate sol-gel by combining Y and Fe with the molar ratio 3:5 [45]. The lattice parameters of YIn(Mn)O₃ pigments synthesized by Rosati et al. [31] are similar to those measured in this study (see Table 3). This is due to the fact that the ionic radius of Mn³⁺ (0.066–0.067 nm) and Fe³⁺ (0.064 nm) are in close proximity [65].

The visible reflectance spectra of the pigments and ZnO powder (Fig. 6a) reveal nearly complete reflectance for ZnO (represented by the grey spectrum) and a broad absorption band spanning the entire visible range for the YInFeO based powders. As expected, the inclusion of ZnO leads to an enhancement in reflectance (notice the increase in reflectance for the curves corresponding to the YInFeO MIX ZnO and YInFeO-ZnO samples). The visible reflectance spectra were employed to extract the colorimetric coordinates according to the CIE-1976 Lab* color space [40]. The CIE-1976 L*a*b* colorimetric coordinates are reported in Table S1. Fig. 6b represents a digital reconstruction of the color of the synthesized pigments from the colorimetric coordinates reported in Table S1 as L*a*b* color space coordinates. According to Table S1, zinc

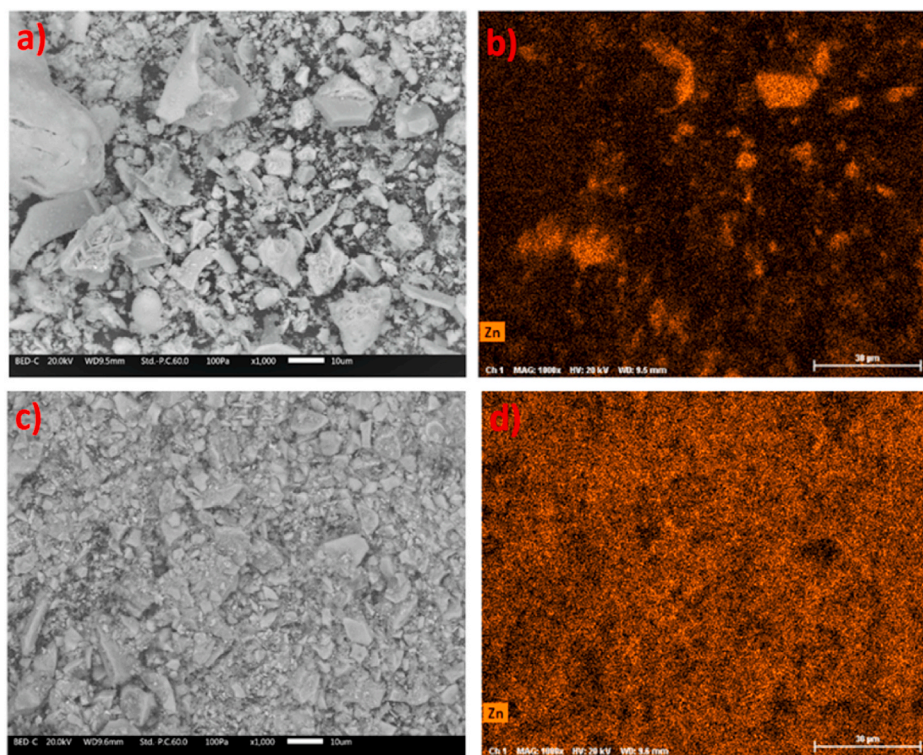


Fig. 4. SEM pictures of YInFeO - ZnO (a) with the corresponding EDXS elemental distribution of Zn (b), and SEM pictures of YInFeO MIX ZnO (c) with the corresponding EDXS elemental distribution of Zn (d).

oxide shows the highest value of L^* while the most saturated color is the pigment $\text{YIn}_{0.9}\text{Fe}_{0.1}\text{O}_3$, without zinc oxide. Looking at the b^* component, it is interesting that zinc oxide addition in the sol-gel bath leads to an increase in b^* (24.68), while the physical mixing causes a decrease in b^* (17.68). The L^* , a^* and b^* values collected for ZnO are in agreement with previous literature reports [66]. Fig. 6b shows that the absence of ZnO results in a deep yellow hue, while the presence of ZnO contributes to a color shift towards blue, resulting in a paler yellow shade.

Fig. 7 displays the near-infrared reflectance profiles of the investigated pigments, with the corresponding solar reflectance spectra presented in Fig. S4. A marginal elevation in NIR reflectance is noticeable in the mixed samples compared to YInFeO. This increase is particularly noteworthy since the 700–1100 nm range is the most critical heat-producing region within the NIR domain [67]. Up to 1100 nm, the samples with ZnO have NIR reflectance spectra that are well stacked, and the reflectance is slightly higher than the reflectance spectrum of YInFeO sample. The notable NIR reflectance exhibited by each pigment is attributed to the inclusion of ZnO, a material known for its high NIR reflectance. This characteristic is evident in the spectrum obtained in Fig. 7 and is corroborated by existing literature [68]. A slight increase above 100 % in reflectance is observed in YInFeO MIX ZnO sample up to about 105 % at the 1750–2500 nm range. This is not unusual when analysing powdery materials in the high wavelengths region of the spectra [9,19,69,70], and is attributed to the housing of the powders in the cuvette.

Comparing data in Fig. 7 and Table 4 there is no marked difference in reflectance between YInFeO - ZnO, with large ZnO crystals, and YInFeO MIX ZnO with nanometric ZnO. The numerical values in Table 4 suggest that YInFeO can reflect near-infrared radiation similarly to pigments with ZnO, according to the NIR reflectance spectrum of YInFeO in Fig. 7. The reflectance values are close to those of the other spectra at 1100 nm (see values in column IR reflectance at 1100 nm (%) in Table 4). Thus, NIR reflectance is mainly intrinsic in YInFeO, according to the findings of other authors [71].

Table 5 presents a comparison of the color and NIR reflectance

properties between the materials synthesized in this study and yellow pigments developed by other authors. It is noteworthy that the NIR reflectance values obtained in our study are comparable or slightly lower when compared to pigments developed by other authors. Concerning the yellow hue, the incorporation of Bi into the crystalline structure of the compound results in a vivid coloration, as indicated by high and positive values of the coordinate b^* . However, it is important to highlight that the materials developed in this work often exhibit similarity to other pale yellow pigments developed by different researchers.

The photocatalytic performance of the pigments was evaluated by observing the degradation of 4-Nitrophenol (4-NP) under UV light exposure. The YInFeO sample exhibited no discernible photochemical activity. In contrast, the presence of ZnO facilitated the nearly complete degradation of 4-NP within approximately 120 min, according to the relevant literature [14]. ZnO promotes the almost complete degradation of 4-NP after about 120 min. Coupling ZnO with YInFeO improves the degradation efficiency with respect to simply ZnO when the components are mechanically mixed, while lower photochemical activity can be observed for the YInFeO-ZnO sample.

The diminished photochemical activity observed in the YInFeO sample can likely be ascribed to the enlargement of ZnO particle size during synthesis (as depicted in Fig. 4), resulting in a reduction in the exposed surface area. Additionally, XRD results underscore the growth of YInFeO particles on the surface of ZnO, which further diminishes the direct interaction between the active surface of ZnO and the target pollutant. On the other hand, when ZnO and YInFeO are mixed, the size distribution of the ZnO particles is maintained, thus resulting in improved photocatalytic efficiency. Notably, the mechanical mixture is slightly more active than bare ZnO, even if the amount of the ZnO is about 30 wt% lower in the reacting mixture. This implies the possibility of a synergistic effect between the two components, although further research is needed to validate this hypothesis.

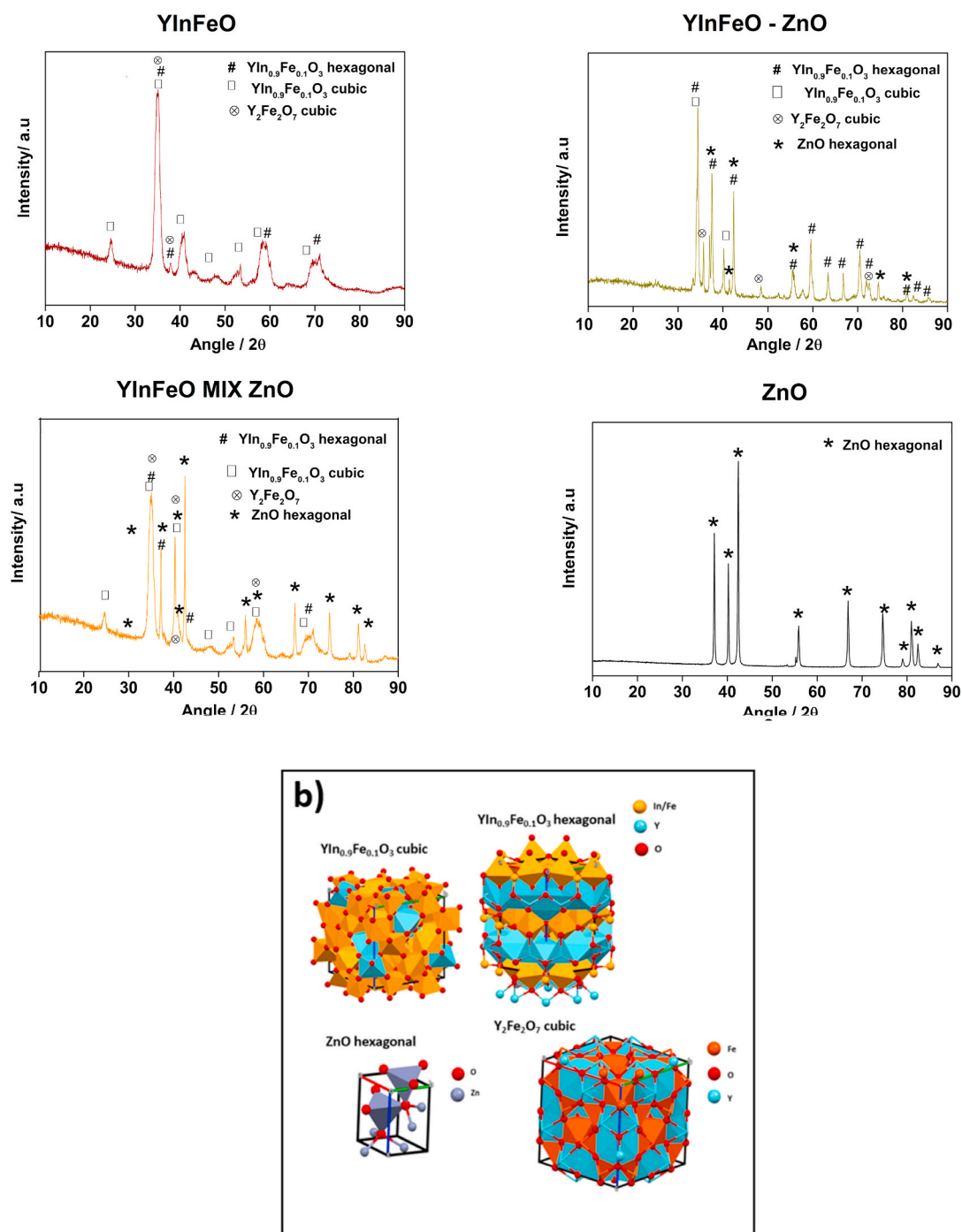


Fig. 5. X-ray diffraction (XRD) patterns of the pigments under investigation (a) and their corresponding crystalline structures (b).

3.2. Coatings

The colorimetric coordinates for the coatings are provided in Table S2 and depicted within the CIE-1976 Lab* color space in Fig. 9a. The distinction between the presence and absence of ZnO is likewise discernible when the pigments are incorporated into the polymeric matrix. In fact, ZnO increases the reflectance (Fig. 9b) and L* component of coatings, shifting to a lighter yellow hue. As reported in Table S2 and Fig. 9, the absence of ZnO makes a more saturated yellow color, with the lowest L* (64.61) and the highest b* (31.72). The colorimetric coordinates of the coatings exhibit more significant variations compared to the corresponding pigments. Therefore, it appears that the binder enhances the contrast in the various colors. The visible reflectance spectra

of coatings YInFeO ZnO + binder and YInFeO MIX ZnO + binder are similar to those of ZnO + binder beyond 600 nm. This is further evidence of the fact that the presence of ZnO modifies color shades.

High-contrast SEM pictures of the different coatings were collected to evaluate the distribution of the particles inside the binder, through a binary area fraction plot (Fig. 10). Binary area fraction plots were employed to investigate the particle distribution in polymeric matrixes [78–80]. The histograms of the plot are obtained by calculating the total area occupied by the pigments (the area corresponding to the high-contrast white particles). The binary area fraction values, derived from SEM pictures, suggest a homogeneous distribution of pigments inside the matrix in all the investigated coatings (see numerical values in Table S2).

Table 3
Crystallographic data of the synthesized pigments.

	Reliability factors (%)		YIn _{0.9} Fe _{0.1} O ₃ Phases				ZnO Phase			Y ₂ Fe ₂ O ₇ Phase		
	R _{wp}	R _{exp}	Cubic (Space group Ia-3)		Hexagonal (Space group P6 ₃ cm)		Hexagonal (Space group P6 ₃ mc)			Cubic (Space group F23)		
			Cell parameters (Å)	Amount (%)	Cell parameters (Å)		Amount (%)	Cell parameters (Å)		Amount (%)	Cell parameters (Å)	Amount (%)
					a	c		a	c			
YInFeO ₃	12.92	4.20	10.4558 ±0.0020	93.76 ±14.00	6.2698 ±0.0003	12.1879 ±0.0122	5.65 ±1.72			10.3007 ±0.0023	0.58 ±0.09	
YInFeO - ZnO	29.21	7.47	10.6318 ±0.0004	16.42 ±1.64	6.2776 ±0.0008	12.2519 ±0.0003	56.21 ±3.34	3.2495 ±0.0006	5.2295 ±0.0020	26.75 ±0.01	10.1810 ±0.0027	0.60 ±0.06
YInFeO MIX ZnO	16.88	4.39	10.4145 ±0.0002	75.30 ±1.93	6.2648 ±0.0021	2.4454 ±0.0019	2.51 ±0.25	3.2665 ±0.0007	5.2051 ±0.0001	21.81 ±0.01	10.2861 ±0.0020	0.36 ±0.03
ZnO								3.2492 ±0.0006	5.2055 ±0.0001	100 ±0.01		

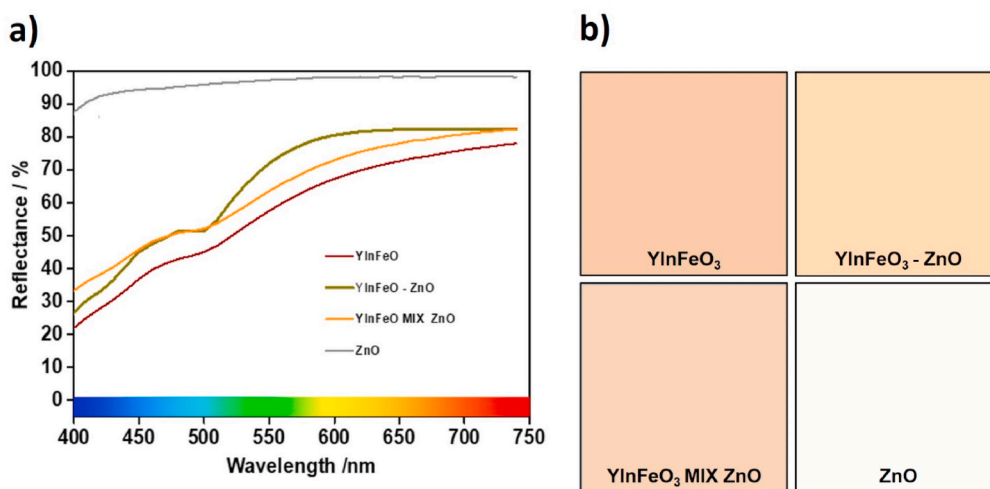


Fig. 6. Visible reflectance spectra (a) and digital reconstruction of the colors of the investigated pigments obtained from the CIE-1976 L*a*b* colorimetric coordinates (b).

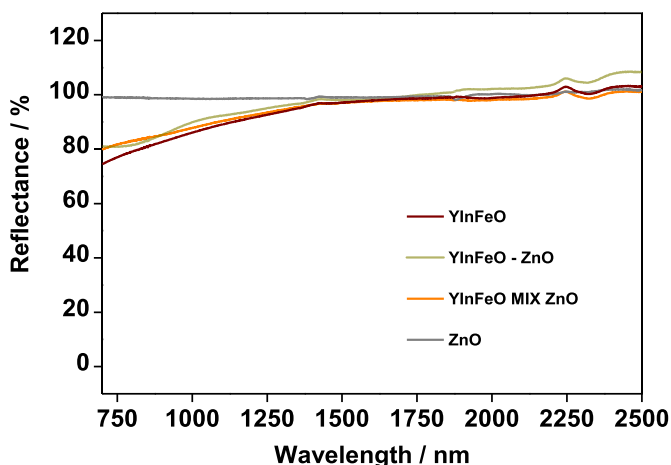


Fig. 7. Spectral profiles of near-infrared (NIR) reflectance for the examined pigments.

In all the investigated coatings, the pigments seem well dispersed and show the same degree of distribution. As revealed by the SEM pictures of the pigments, the shape of the synthesized pigments is not homogeneous while samples ZnO + binder and TiO₂ + binder (Fig. 10) show uniform particles.










Table 4
Solar reflectance and NIR reflectance at 1100 nm of the investigated pigments.

Pigments	Solar reflectance, R* (%)	IR reflectance at 1100 nm (%)
YInFeO ₃	85.5	89.3
YInFeO - ZnO	88.4	92.5
YInFeO MIX ZnO	89.0	90.5
ZnO	100.2	98.9

Fig. 11 displays the near-infrared (NIR) reflectance spectra of the pigmented coatings in comparison to the reference samples. Similarly to the NIR reflectance spectra of the pigments, the NIR reflectance at 1100 nm can describe the feasibility of the developed coatings as cool-roof materials. From the comparison of the spectra, it is possible to note that the coatings maintain almost the same behaviour than the pigments. Differently from the reflectance spectra of the synthesized pigments, the difference between coatings containing ZnO (YInFeO ZnO + binder, YInFeO MIX ZnO + binder, ZnO + binder) and coatings without it (YInFeO + binder) is more marked. The YInFeO + binder coating exhibits a noteworthy reduction in NIR reflectance, extending up to 1100 nm.

The NIR solar reflectance power spectra of the analyzed coatings, obtained in accordance with ASTM G173-03 standards (as depicted in Fig. S5), confirm the trend observed in NIR reflectance. These outcomes can be explained considering that NIR reflectance is primarily

Table 5
Comparison of the color coordinates and the NIR reflectance of yellow pigments.

Chemical compound	Color coordinates			Color (from color coordinates)	NIR Reflectance (R %)	Reference
	L*	a*	b*			
BiVO ₄ -ZnO	86.79	4.92	53.50		99.6	[64]
CeBi ₁₅ O ₂₄	80.51	6.62	52.26		≈87.0	[72]
Yb ₆ Mo ₂ O ₁₅	95.20	-11.70	28.30		93.7	[73]
Bi _{1.50} Y _{0.50} Ce ₂ O ₇	76.85	13.33	47.97		91.9	[74]
Bi _{1.20} Er _{0.80} MoO ₆	81.70	4.99	34.41		96.9	[75]
[(Li _{0.4} Lu _{0.6} Al _{0.6}) _{0.1} Bi _{0.8}][Mo _{0.2} V _{0.8}]O ₄	83.40	8.85	79.29		97.6	[76]
BiP _{0.9} V _{0.1} O ₄	91.33	-3.51	27.15		90.2	[77]
YInFeO ₃	80.17	5.51	22.63		89.3	This work
YInFeO - ZnO	86.52	4.56	24.58		92.5	This work

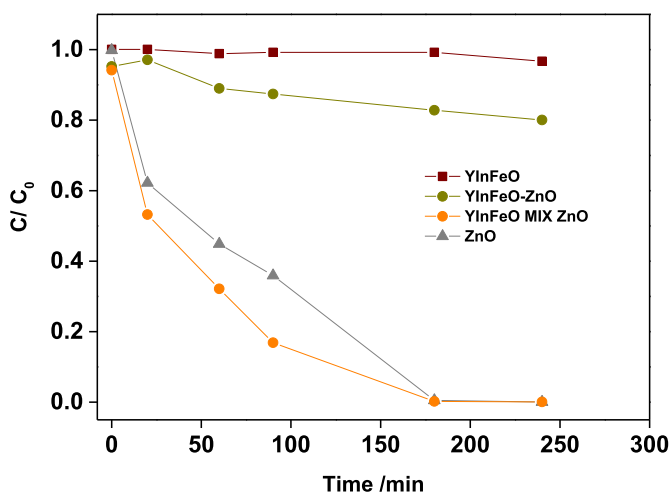


Fig. 8. The concentration of 4-Nitrophenol as a function of UV light irradiation time in the presence of the synthesized pigments.

influenced by the presence of ZnO, which imparts the highest values of IR reflectance (%) at 1100 nm and solar reflectance (R^*), as reported in Table 6.

According to the data reported in Table 6, the calculated solar reflectance R^* is lower for the coating containing solely YIn_{0.9}Fe_{0.1}O₃ (60.65 %) and increases with the addition of ZnO in the binder. For the coating YInFeO MIX ZnO + binder, R^* is the highest (68.95 %) among the samples containing the synthesized pigments (excluding the sample TiO₂ + binder, $R^* = 79.9\%$). Comparing the numerical values in Table 6 (R^* and IR reflectance at 1100 nm) there are no marked differences in R^* for the samples YInFeO MIX ZnO + binder and YInFeO-ZnO + binder (66.1 % and 68.95 %, respectively). R^* value for ZnO is 70.5 %, similar to those of YInFeO - ZnO + binder and YInFeO MIX ZnO + binder. The bare AA5005 substrate exhibits NIR reflectance values of 40% across the entire NIR spectrum. The TiO₂ + binder and Graphite + binder coatings validate their suitability as control samples: TiO₂ + binder stands out as the most reflective sample with an R^* of 79.9%. Conversely, Graphite +

binder is the sample with very low NIR reflectance ($R^* = 8.50\%$), in agreement with the literature [81].

The temperature (T_{panel}) of the different coatings exposed to the xenon arc lamp is reported in Fig. 12. For the YInFeO + binder sample, T_{panel} is 67.0 °C. This temperature decreases adding ZnO: YInFeO - ZnO + binder coating ($T_{\text{panel}} = 66.3$ °C) and YInFeO MIX ZnO + binder coating ($T_{\text{panel}} = 64.5$ °C), shows lower panel temperature. The incorporation of YIn_{0.9}Fe_{0.1}O₃ and ZnO particles can be deduced to assist in alleviating the temperature increase. Hence, the pigments synthesized in this study can be employed in the development of cool materials.

We evaluated the photocatalytic performance of the pigments incorporated into the acrylic binder by assessing the degradation of both 4-NP and methylene blue (MB). The Xenon Arc Lamp was employed for the test. The two reference samples (TiO₂ + binder and simply clear-coat), were also tested for comparison. All the examined pigments demonstrated equivalent efficacy in degrading the target pollutants. Fig. 13 reports, for example, the evolution of the degradation curve for 4-NP and MB in contact with the coating containing YInFeO MIX ZnO. The decrease in concentration values of all samples were used to calculate an average value of C/C_0 at each time. None of the investigated coatings induced a complete degradation of 4-NP, regardless of the embedded pigments. Even prolonged irradiation time (up to 420 h, not shown) was not sufficient to promote complete degradation of the molecule. Taking into account the photocatalytic outcomes observed with the pigments (as shown in Fig. 8), this phenomenon can be attributed to the acrylic binder, which significantly restricts the direct interaction between 4-NP and the pigments, thereby inhibiting interfacial electron transfer and the generation of reactive oxygen species. Therefore, even if adding ZnO endows the pigment with both efficient NIR adsorption and photocatalytic activity, the binder/pigments interactions should be further deepened and improved. On the other hand, MB concentration in the solution decreased with the same trend in the presence of all of the embedded pigments and the acrylic binder without pigments. These results highlight that, as also reported elsewhere in the literature [82,83], MB is not a suitable compound to test the activity of coatings because of the complex photochemistry and the plethora of photoinduced mechanisms which can take place concurrently to the direct photocatalytic one, which is the target to be investigated when testing the activity of photoactive materials.

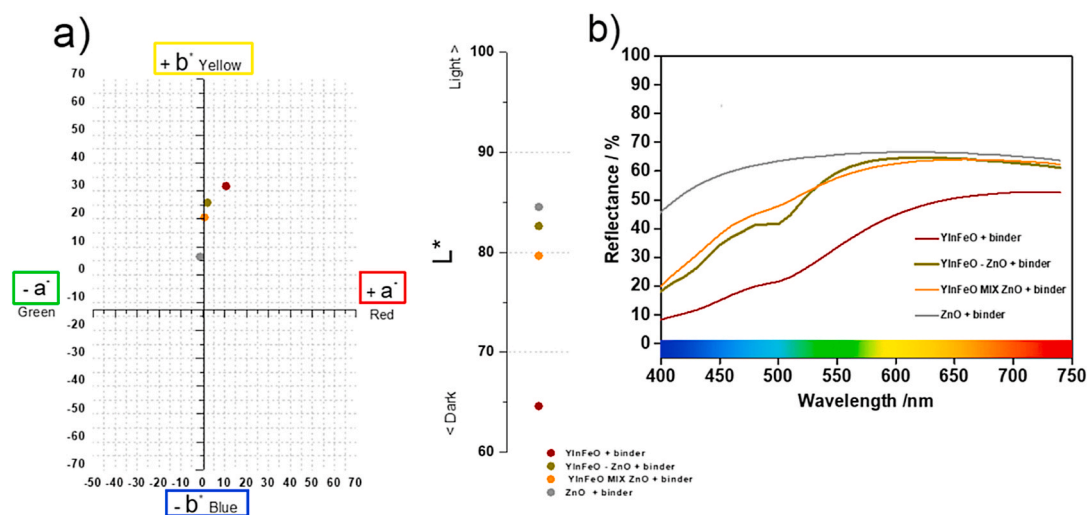


Fig. 9. Colorimetric coordinates values for derived coatings, in CIE-1976 L*a*b* color space (a) and visible light reflectance spectra (b).

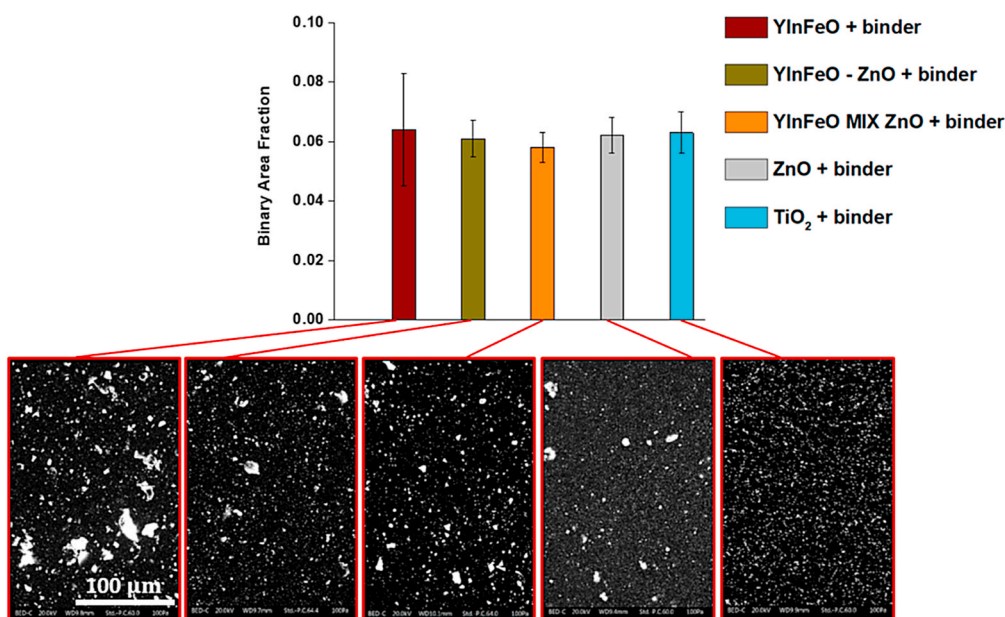


Fig. 10. Measured binary area fraction: graphical representation of the amount of pigment particles inside the acrylic binder; the high contrast SEM pictures are shown on the bottom of the plot.

4. Conclusions

YIn_{0.9}Fe_{0.1}O₃ based pigments were synthesized through an environmentally friendly chemical route. Simply YIn_{0.9}Fe_{0.1}O₃ showed intrinsic NIR reflective properties but very limited photochemical activity. The YInFeO₃ mixed with ZnO nanoparticles has been found to be a promising pigment able to reflect NIR radiation, cool down the temperature of the coating, and show photocatalytic activity even higher than bare ZnO. Interestingly, the NIR reflectance of simply YIn_{0.9}Fe_{0.1}O₃ is comparable to that of YIn_{0.9}Fe_{0.1}O₃ mixed with ZnO. However, the latter modifies the color shades and increases the photocatalytic properties.

Mechanically mixing YIn_{0.9}Fe_{0.1}O₃ with ZnO yields superior outcomes compared to the direct synthesis of the composite, particularly in terms of photocatalytic activity. NIR reflectance spectra and the R* values of the YIn_{0.9}Fe_{0.1}O₃ pigment, which are comparable to those of pigments containing ZnO, underscore that the elevated NIR reflectance values are not solely attributed to ZnO but also arise from the inherent

properties of YIn_{0.9}Fe_{0.1}O₃.

Considering all synthesized pigments, when they are added to an acrylic binder, they can confer the features of a cool coating to a layer (high NIR reflectance and low temperature of the coating). However, when the pigments are embedded in the acrylic binder, the photocatalytic activity is almost completely suppressed, probably because the polymeric binder incorporates the particles completely. Additional research is currently underway to develop coating materials capable of providing adequate mechanical properties while maintaining the photocatalytic activity of the pigments and the cooling effect. Furthermore, it has been emphasized that the utilization of methylene blue can yield deceptive results when assessing the photocatalytic activity of such materials.

Data availability

The raw/processed data required to reproduce these findings cannot be shared at this time due to technical or time limitations.

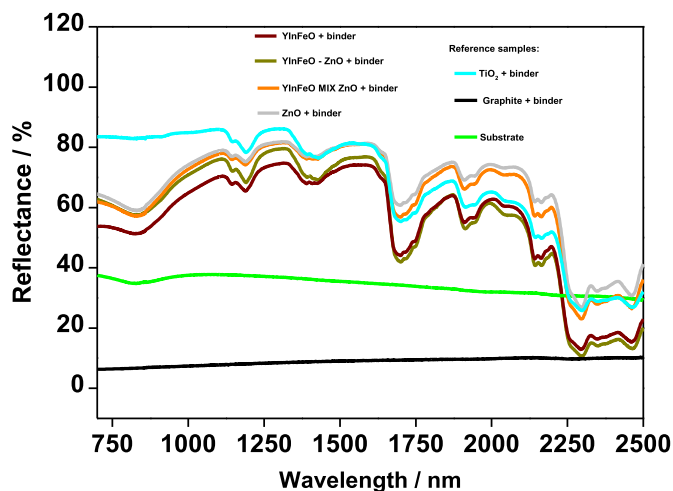


Fig. 11. Near-infrared (NIR) reflectance of the coatings under investigation.

Table 6

Solar reflectance and NIR reflectance at 1100 nm of the investigated coatings.

Samples	Solar reflectance R* (%)	IR reflectance at 1100 nm (%)
YinFeO + binder	60.6	69.7
YinFeO - ZnO + binder	66.1	75.6
YinFeO MIX ZnO + binder	68.9	77.0
ZnO + binder	70.5	79.0
TiO ₂ + binder	80.0	85.8
Graphite + binder	8.5	7.6
Substrate	36.3	37.6

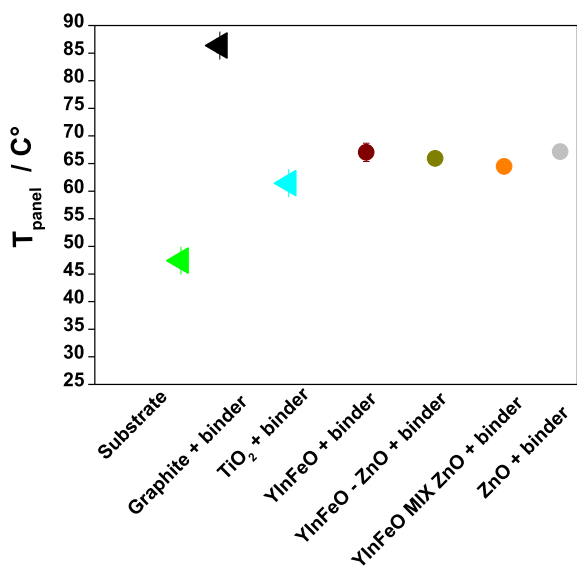


Fig. 12. The mean temperature of the rear surface of the panel, T_{panel} (°C) measured upon exposure to the Xenon Arc Lamp.

Declaration of competing interest

The authors declare that they have no known competing financial interests or personal relationships that could have appeared to influence the work reported in this paper.

Appendix A. Supplementary data

Supplementary data to this article can be found online at <https://doi.org/10.1016/j.ceramint.2024.02.075>.

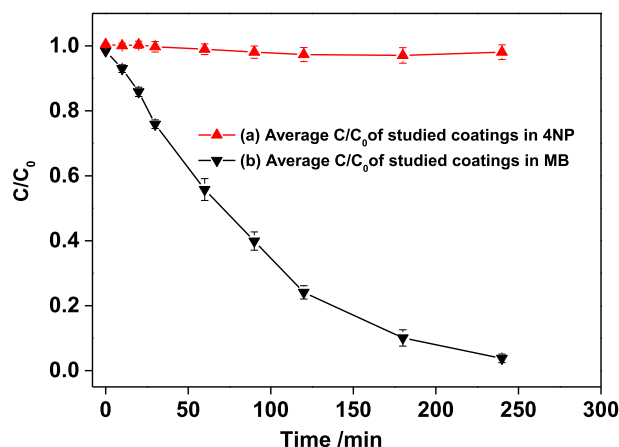


Fig. 13. Concentration of MB and 4-NP versus irradiation time under the xenon arc lamp in the presence of the YinFeO MIX ZnO pigment.

[org/10.1016/j.ceramint.2024.02.075](https://doi.org/10.1016/j.ceramint.2024.02.075).

References

- [1] D. Guilbert, S. Caluwaerts, K. Calle, N. Van Den Bossche, V. Cnudde, T. De Kock, Impact of the urban heat island on freeze-thaw risk of natural stone in the built environment, a case study in Ghent, Belgium, *Sci. Total Environ.* 677 (2019) 9–18, <https://doi.org/10.1016/j.scitotenv.2019.04.344>.
- [2] W. Wang, K. Liu, R. Tang, S. Wang, Remote sensing image-based analysis of the urban heat island effect in Shenzhen, China, *Phys. Chem. Earth* 110 (2019) 168–175, <https://doi.org/10.1016/j.pce.2019.01.002>.
- [3] J. Jazaeri, R.L. Gordon, T. Alpcan, Influence of building envelopes, climates, and occupancy patterns on residential HVAC demand, *J. Build. Eng.* 22 (2019) 33–47, <https://doi.org/10.1016/j.jobbe.2018.11.011>.
- [4] U. Berardi, A.A. Gallardo, Properties of concretes enhanced with phase change materials for building applications, *Energy Build.* 199 (2019) 402–414, <https://doi.org/10.1016/j.enbuild.2019.07.014>.
- [5] S. Nandja, A. Haché, Attenuated internal reflection at an interface with a phase change material, *Opt Commun.* 449 (2019) 63–68, <https://doi.org/10.1016/j.optcom.2019.05.029>.
- [6] T. Kolás, A. Røyset, M. Grandcolas, M. ten Cate, A. Lacau, Cool coatings with high near infrared transmittance for coil coated aluminium, *Sol. Energy Mater. Sol. Cells* 196 (2019) 94–104, <https://doi.org/10.1016/j.solmat.2019.03.021>.
- [7] K.L. Uemoto, N.M.N. Sato, V.M. John, Estimating thermal performance of cool colored paints, *Energy Build.* 42 (2010) 17–22, <https://doi.org/10.1016/j.enbuild.2009.07.026>.
- [8] R.L. Å, P. Berdahl, H. Akbari, Solar spectral optical properties of pigments — Part II, survey of common colorants 89 (2005) 351–389, <https://doi.org/10.1016/j.solmat.2004.11.013>.
- [9] Y.F. Gomes, J. Li, K.F. Silva, A.A.G. Santiago, M.R.D. Bomio, C.A. Paskocimas, M. A. Subramanian, F. V. Motta, Synthesis and characterization of Y (In, Mn) O₃ blue pigment using the complex polymerization method (CPM), *Ceram. Int.* 44 (2018) 11932–11939, <https://doi.org/10.1016/j.ceramint.2018.04.152>.
- [10] S. Sadeghi-Niaraki, B. Ghasemi, A. Habibolahzadeh, E. Ghasemi, M. Ghahari, Nanostructured Fe₂O₃@TiO₂ pigments with improved NIR reflectance and photocatalytic ability, *Mater. Chem. Phys.* 235 (2019) 121769, <https://doi.org/10.1016/j.matchemphys.2019.121769>.
- [11] S. Jose, A. Jayaprakash, S. Laha, S. Natarajan, K.G. Nishanth, M.L.P. Reddy, YIn_{0.9}Mn_{0.1}O₃-ZnO nano-pigment exhibiting intense blue color with impressive solar reflectance, *Dyes Pigments* 124 (2016) 120–129, <https://doi.org/10.1016/j.dyepig.2015.09.014>.
- [12] F. Parrino, C. De Pasquale, L. Palmisano, Influence of surface-related phenomena on mechanism, selectivity, and conversion of TiO₂-induced photocatalytic reactions, *ChemSusChem* 12 (2019) 589–602.
- [13] H. Lachheb, F. Ajala, A. Hamrouni, A. Houas, F. Parrino, L. Palmisano, Electron transfer in ZnO-Fe₂O₃ aqueous slurry systems and its effects on visible light photocatalytic activity, *Catal. Sci. Technol.* 7 (2017) 4041–4047.
- [14] A. Hamrouni, N. Mousa, A. Di Paola, L. Palmisano, A. Houas, F. Parrino, Photocatalytic activity of binary and ternary SnO₂-ZnO-ZnWO₄ nanocomposites, *J. Photochem. Photobiol. Chem.* 309 (2015) 47–54, <https://doi.org/10.1016/j.jphotochem.2015.05.001>.
- [15] A. Hamrouni, H. Azzouzi, A. Rayes, L. Palmisano, R. Ceccato, F. Parrino, Enhanced solar light photocatalytic activity of Ag doped TiO₂-Ag₃PO₄ composites, *Nanomaterials* 10 (2020) 795.
- [16] M. Pirhashemi, A. Habibi-Yangjeh, S. Rahim Pouran, Review on the criteria anticipated for the fabrication of highly efficient ZnO-based visible-light-driven photocatalysts, *J. Ind. Eng. Chem.* 62 (2018) 1–25, <https://doi.org/10.1016/j.jiec.2018.01.012>.

- [17] H. Tada, Q. Jin, H. Nishijima, H. Yamamoto, M. Fujishima, S. Okuoka, T. Hattori, Y. Sumida, H. Kobayashi, Titanium(IV) dioxide surface-modified with iron oxide as a visible light photocatalyst, *Angew. Chemie Int. Ed.* 50 (2011) 3501–3505, <https://doi.org/10.1002/anie.201007869>.
- [18] J. Liu, S. Yang, W. Wu, Q. Tian, S. Cui, Z. Dai, F. Ren, X. Xiao, C. Jiang, 3D flowerlike α -Fe₂O₃@TiO₂ Core-shell nanostructures: general synthesis and enhanced photocatalytic performance, *ACS Sustain. Chem. Eng.* 3 (2015) 2975–2984, <https://doi.org/10.1021/acsuschemeng.5b00956>.
- [19] J. Li, M.A. Subramanian, Inorganic pigments with transition metal chromophores at trigonal bipyramidal coordination: Y(In,Mn)O₃ blues and beyond, *J. Solid State Chem.* 272 (2019) 9–20, <https://doi.org/10.1016/j.jssc.2019.01.019>.
- [20] Y. Zhang, J. Yang, J. Xu, Q. Gao, Z. Hong, Controllable synthesis of hexagonal and orthorhombic YFeO₃ and their visible-light photocatalytic activities, *Mater. Lett.* 81 (2012) 1–4, <https://doi.org/10.1016/j.matlet.2012.04.080>.
- [21] M. Ismael, E. Elhaddad, D.H. Taffa, M. Wark, Synthesis of phase pure hexagonal YFeO₃ perovskite as efficient visible light active photocatalyst, *Catal* 7 (2017), <https://doi.org/10.3390/catal7110326>.
- [22] Y.-H. Liu, Y.-S. Kuo, W.-C. Liu, W.-L. Chou, Photoelectrocatalytic activity of perovskite YFeO₃/carbon fiber composite electrode under visible light irradiation for organic wastewater treatment, *J. Taiwan Inst. Chem. Eng.* 128 (2021) 227–236, <https://doi.org/10.1016/j.jtice.2021.08.029>.
- [23] M. Ismael, E. Elhaddad, D.H. Taffa, M. Wark, Solid state route for synthesis of YFeO₃/g-C₃N₄ composites and its visible light activity for degradation of organic pollutants, *Catal. Today* 313 (2018) 47–54, <https://doi.org/10.1016/j.cattod.2018.02.003>.
- [24] M. Fortuño-Morte, P. Serna-Gallén, H. Beltrán-Mir, E. Condoncillo, A new series of environment-friendly reddish inorganic pigments based on AFeO₃ (A = Ln, Y) with high NIR solar reflectance, *J. Mater.* 7 (2021) 1061–1073, <https://doi.org/10.1016/j.jmat.2021.02.002>.
- [25] Y. Li, Y. Ma, W. Liu, Z. Wang, H. Liu, X. Wang, H. Wei, S. Zeng, N. Yi, G.J. Cheng, A promising inorganic YFeO₃ pigments with high near-infrared reflectance and infrared emission, *Sol. Energy* 226 (2021) 180–191, <https://doi.org/10.1016/j.solener.2021.08.047>.
- [26] J. Li, U.G. Singh, T.D. Schladt, J.K. Stalick, S.L. Scott, R. Seshadri, Hexagonal YFe_{1-x}Pd_xO_{3-δ}: nonperovskite host compounds for Pd²⁺ and their catalytic activity for CO oxidation, *Chem. Mater.* 20 (2008) 6567–6576, <https://doi.org/10.1021/cm801534a>.
- [27] P. Vaqueiro, M.A. López-Quintela, Influence of complexing agents and pH on yttrium–iron garnet synthesized by the sol–gel method, *Chem. Mater.* 9 (1997) 2836–2841, <https://doi.org/10.1021/cm970165f>.
- [28] A. Rosati, M. Fedel, S. Rossi, NIR reflective pigments for cool roof applications: a comprehensive review, *J. Clean. Prod.* 313 (2021) 127826, <https://doi.org/10.1016/j.jclepro.2021.127826>.
- [29] P.-K. Lee, S. Yu, H.J. Chang, H.Y. Cho, M.-J. Kang, B.-G. Chae, Lead chromate detected as a source of atmospheric Pb and Cr (VI) pollution, *Sci. Rep.* 6 (2016), <https://doi.org/10.1038/srep36088>.
- [30] S.D. Dolić, D.J. Jovanović, D. Štrbac, L.D. Far, M.D. Dramićanin, Improved coloristic properties and high NIR reflectance of environment-friendly yellow pigments based on bismuth vanadate, *Ceram. Int.* 44 (2018) 22731–22737, <https://doi.org/10.1016/j.ceramint.2018.09.057>.
- [31] A. Rosati, M. Fedel, S. Rossi, YIn_{0.9}Mn_{0.1}O₃–ZnO NIR reflective nano-pigment exhibiting three different colors: ochre, cyan blue, and deep blue, *J. Solid State Chem.* (2021) 122176, <https://doi.org/10.1016/j.jssc.2021.122176>.
- [32] M.V. Diamanti, R. Paolini, M. Rossini, A.B. Aslan, M. Zinzi, T. Poli, M.P. Pedferri, Long term self-cleaning and photocatalytic performance of anatase added mortars exposed to the urban environment, *Construct. Build. Mater.* 96 (2015) 270–278, <https://doi.org/10.1016/j.conbuildmat.2015.08.028>.
- [33] S. Kinoshita, A. Yoshida, Investigating performance prediction and optimization of spectral solar reflectance of cool painted layers, *Energy Build.* 114 (2016) 214–220, <https://doi.org/10.1016/j.enbuild.2015.06.072>.
- [34] A.P. Werle, M.L. De Souza, K. Loh, R. Ando, V.M. John, The performance of a self-cleaning cool cementitious surface, *Energy Build.* 114 (2016) 200–205, <https://doi.org/10.1016/j.enbuild.2015.06.025>.
- [35] H. Badenhorst, N. Fox, A. Mutalib, The use of graphite foams for simultaneous collection and storage of concentrated solar energy, *Carbon N. Y.* 99 (2016) 17–25, <https://doi.org/10.1016/j.carbon.2015.11.071>.
- [36] M. Chandrashekhara, A. Yadav, Experimental study of exfoliated graphite solar thermal coating on a receiver with a Scheffler dish and latent heat storage for desalination, *Sol. Energy* 151 (2017) 129–145, <https://doi.org/10.1016/j.solener.2017.05.027>.
- [37] L. Lutterotti, S. Matthies, H.R. Wenk, MAUD: a friendly Java program for material analysis using diffraction, *IUCr: Newsletter of the CPD 21* (1999) 14–15.
- [38] L. Lutterotti, M. Bortolotti, Object Oriented Programming and Fast Computation Techniques in Maud, a Program for Powder Diffraction Analysis Written in Java TM, vol. 2, 2003, pp. 43–50.
- [39] ASTM, Standard tables for reference solar spectral irradiances : direct normal and, *astm*, 03, <https://doi.org/10.1520/G0173-03R20.2>, 2013.
- [40] K. McLAREN, XIII—the development of the CIE 1976 (L* a* b*) uniform colour space and colour-difference formula, *J. Soc. Dye. Colour.* 92 (1976) 338–341, <https://doi.org/10.1111/j.1478-4408.1976.tb03301.x>.
- [41] A. Rosati, M. Fedel, S. Rossi, Laboratory scale characterization of cool roof paints: comparison among different artificial radiation sources, *Prog. Org. Coating* 161 (2021) 106464, <https://doi.org/10.1016/j.porgcoat.2021.106464>.
- [42] P.N.M. Dos Anjos, E.C. Pereira, Y.G. Gobato, Study of the structure and optical properties of rare-earth-doped aluminate particles prepared by an amorphous citrate sol-gel process, *J. Alloys Compd.* 391 (2005) 277–283, <https://doi.org/10.1016/j.jallcom.2004.08.058>.
- [43] S. Vivekanandhan, M. Venkateswarlu, N. Satyanarayana, Synthesis and characterization of nanocrystalline LiNi_{0.5}Co_{0.5}VO₄ powders by citric acid assisted sol-gel combustion process, *J. Alloys Compd.* 462 (2008) 328–334, <https://doi.org/10.1016/j.jallcom.2007.08.055>.
- [44] S. Yu, W. Jing, M. Tang, T. Xu, W. Yin, B. Kang, Fabrication of Nd:YAG transparent ceramics using powders synthesized by citrate sol-gel method, *J. Alloys Compd.* 772 (2019) 751–759, <https://doi.org/10.1016/j.jallcom.2018.09.184>.
- [45] S. Hosseini Vajargah, H.R. Madaah Hosseini, Z.A. Nemat, Preparation and characterization of yttrium iron garnet (YIG) nanocrystalline powders by auto-combustion of nitrate-citrate gel, *J. Alloys Compd.* 430 (2007) 339–343, <https://doi.org/10.1016/j.jallcom.2006.05.023>.
- [46] M. Blosi, S. Albonetti, M. Dondi, A. Costa, M. Ardit, G. Cruciani, Sol-gel combustion synthesis of chromium doped yttrium aluminum perovskites, *J. Sol. Gel Sci. Technol.* 50 (2009) 449–455, <https://doi.org/10.1007/s10971-009-1906-5>.
- [47] C.Y. Kim, T. Sekino, K. Niihara, Synthesis of bismuth sodium titanate nanosized powders by solution, sol – gel process 67 (2003) 1464–1467.
- [48] T.H. Dolla, K. Pruessner, D.G. Billing, C. Sheppard, A. Prinsloo, E. Carleschi, B. Doyle, P. Ndungu, Sol-gel synthesis of Mn_xNi_{1-x}Co₂O₄ spinel phase materials: structural, electronic, and magnetic properties, *J. Alloys Compd.* 742 (2018) 78–89, <https://doi.org/10.1016/j.jallcom.2018.01.139>.
- [49] N. Brahme, A. Gupta, D.P. Bisen, U. Kurrey, Thermoluminescence study of Y₂O₃: Tb, *Recent Res. Sci. Technol.* 4 (2012) 130–132.
- [50] A.J. Abdulghani, W.M. Al-Ogedy, Preparation and Characterization of yttrium oxide nanoparticles at different calcination temperatures from yttrium hydroxide prepared by hydrothermal and hydrothermal microwave methods, *Ogedy Iraqi J. Sci.* 56 (2015) 1572–1587.
- [51] X. Lü, J. Xie, H. Shu, J. Liu, C. Yin, J. Lin, Microwave-assisted synthesis of nanocrystalline YFeO₃ and study of its photoactivity, *Mater. Sci. Eng. B Solid-State Mater. Adv. Technol.* 138 (2007) 289–292, <https://doi.org/10.1016/j.mseb.2007.01.003>.
- [52] S.R. Naik, A. V Salker, Variation in the magnetic moment of indium doped Ce_{0.1}Y_{2.9}Fe₅O₁₂ garnet relative to the site inversion, *J. Alloys Compd.* 600 (2014) 137–145, <https://doi.org/10.1016/j.jallcom.2014.02.101>.
- [53] A. Kajibafvala, M.R. Shayegh, M. Mazlumi, S. Zanganeh, A. Lak, M.S. Mohajerani, S.K. Sadrmehzaad, Nanostructure sword-like ZnO wires: rapid synthesis and characterization through a microwave-assisted route, *J. Alloys Compd.* 469 (2009) 293–297, <https://doi.org/10.1016/j.jallcom.2008.01.093>.
- [54] M.-K. Lee, T.-H. Shih, P.-C. Chen, Zinc oxide and zinc hydroxide growth controlled by nitric acid in zinc nitrate and hexamethylenetetramine, *J. Electrochem. Soc.* 156 (2009) H268.
- [55] L.Z. Zhao, H.Y. Yu, W.T. Guo, J.S. Zhang, Z.Y. Zhang, M. Hussain, Z.W. Liu, J. M. Greneche, Phase and hyperfine structures of melt-spun nanocrystalline (Ce_{1-x}Nd_x)₁₆Fe₇₈B₆ Alloys, *IEEE Trans. Magn.* 53 (2017) 1–5, <https://doi.org/10.1109/TMAG.2017.2695533>.
- [56] M. Alizadeh, H.A. Ardakani, R. Amini, M.R. Ghazanfari, M. Ghaffari, Structural and phase evolution in mechanically alloyed calcium copper titanate dielectrics, *Ceram. Int.* 39 (2013) 3307–3312, <https://doi.org/10.1016/j.ceramint.2012.10.019>.
- [57] A. Jain, S.P. Ong, G. Hautier, W. Chen, W.D. Richards, S. Dacek, S. Cholia, D. Gunter, D. Skinner, G. Ceder, K.A. Persson, Commentary: the materials project: a materials genome approach to accelerating materials innovation, *Apl. Mater.* 1 (2013) 011002, <https://doi.org/10.1063/1.4812323>.
- [58] R. Shukla, F.N. Sayed, V. Grover, S.K. Deshpande, A. Guleria, A.K. Tyagi, Quest for lead free relaxors in YIn_{1-x}Fe_xO₃ (0.0 ≤ x ≤ 1.0) system: role of synthesis and structure, *Inorg. Chem.* 53 (2014) 10101–10111, <https://doi.org/10.1021/ic5009472>.
- [59] M. Oceana, J.P. Espinós, J.B. Carda, Synthesis, through pyrolysis of aerosols, of YIn_{1-x}Mn_xO₃ blue pigments and their efficiency for colouring glazes, *Dyes Pigments* 91 (2011) 501–507, <https://doi.org/10.1016/j.dyepig.2011.03.009>.
- [60] R. Shukla, V. Grover, S.K. Deshpande, D. Jain, A.K. Tyagi, Synthesis and structural and electrical investigations of a hexagonal Y_{1-x}Gd_xInO₃ (0.0 ≤ x ≤ 1.0) system obtained via metastable C-type intermediates, *Inorg. Chem.* 52 (2013) 13179–13187, <https://doi.org/10.1021/ic402085w>.
- [61] A.E. Smith, H. Mizoguchi, K. Delaney, N.A. Spaldin, A.W. Sleight, M. A. Subramanian, Mn³⁺ in trigonal bipyramidal coordination: a new blue chromophore, *J. Am. Chem. Soc.* 131 (2009) 17084–17086, <https://doi.org/10.1021/ja9080666>.
- [62] J.B. Baxter, E.S. Aydil, Epitaxial growth of ZnO nanowires on a-and c-plane sapphire, *J. Cryst. Growth* 274 (2005) 407–411.
- [63] Q. Kuang, Z.-Y. Jiang, Z.-X. Xie, S.-C. Lin, Z.-W. Lin, S.-Y. Xie, R.-B. Huang, L.-S. Zheng, Tailoring the optical property by a three-dimensional epitaxial heterostructure: a case of ZnO/SnO₂, *J. Am. Chem. Soc.* 127 (2005) 11777–11784.
- [64] P.K. Thejus, K.G. Nishanth, Rational approach to synthesis low-cost BiVO₄–ZnO complex inorganic pigment for energy efficient buildings, *Sol. Energy Mater. Sol. Cells* 200 (2019) 109999, <https://doi.org/10.1016/j.solmat.2019.109999>.
- [65] C.C. Huang, Y.H. Hung, J.Y. Huang, M.F. Kuo, Performance improvement of S-band phase shifter using Al, Mn and Gd doped Y₃Fe₅O₁₂ and sintering optimization, *J. Alloys Compd.* 643 (2015) S193–S198, <https://doi.org/10.1016/j.jallcom.2014.12.123>.
- [66] S. Kim, U. Kim, W.-S. Cho, Color formation mechanism of ceramic pigments synthesized in the TiO₂–SnO–ZnO compounds, *J. Korean Ceram. Soc.* 55 (2018) 368–375.

- [67] A. Wong, W.A. Daoud, H.H. Liang, Y.S. Szeto, Application of rutile and anatase onto cotton fabric and their effect on the NIR reflection/surface temperature of the fabric, *Sol. Energy Mater. Sol. Cells* 134 (2015) 425–437, <https://doi.org/10.1016/j.solmat.2014.12.011>.
- [68] N. Kiomarsipour, R. Shoja Razavi, Hydrothermal synthesis of ZnO nanoparticles with high UV absorption and vis/NIR reflectance, *Ceram. Int.* 40 (2014) 11261–11268, <https://doi.org/10.1016/j.ceramint.2014.03.178>.
- [69] J. Li, E.A. Medina, J.K. Stalick, A.W. Sleight, M.A. Subramanian, Colored oxides with hibonite structure: a potential route to non-cobalt blue pigments, *Prog. Solid State Chem.* 44 (2016) 107–122, <https://doi.org/10.1016/j.progsolidstchem.2016.11.001>.
- [70] N. Zhou, J. Luan, Y. Zhang, M. Li, X. Zhou, F. Jiang, J. Tang, Synthesis of high near infrared reflection wurtzite structure green pigments using Co-doped ZnO by combustion method, *Ceram. Int.* 45 (2019) 3306–3312, <https://doi.org/10.1016/j.ceramint.2018.10.241>.
- [71] Y. Song, W. Chen, X.M. Lim, X. Hu, M. Liu, Q. Zhang, Electronic configuration in d-orbitals of doping elements plays as a key factor in tuning near infrared reflection of $\text{YMn}_{0.9}\text{M}_{0.1}\text{O}_3$ ($M = \text{Cr, Mn, Fe, Co, Al, Ga}$ and In), *J. Solid State Chem.* 273 (2019) 81–84, <https://doi.org/10.1016/j.jssc.2019.02.040>.
- [72] S. Jose, S.B. Narendranath, D. Joshy, N.V. Sajith, M.R. Prathapachandra Kurup, P. Periyat, Low temperature synthesis of NIR reflecting bismuth doped cerium oxide yellow nano-pigments, *Mater. Lett.* 233 (2018) 82–85, <https://doi.org/10.1016/j.matlet.2018.08.136>.
- [73] D. Schildhammer, G. Fuhrmann, L. Petschnig, N. Weinberger, H. Schottenberger, H. Huppertz, Synthesis and characterization of a new high NIR reflective ytterbium molybdenum oxide and related doped pigments, *Dyes Pigments* 138 (2017) 90–99, <https://doi.org/10.1016/j.dyepig.2016.11.024>.
- [74] A.K.V. Raj, P.P. Rao, T.S. Sreena, T.R.A. Thara, Pigmentary colors from yellow to red in $\text{Bi}_2\text{Ce}_2\text{O}_7$ by rare earth ion substitutions as possible high NIR reflecting pigments, *Dyes Pigments* 160 (2019) 177–187, <https://doi.org/10.1016/j.dyepig.2018.08.010>.
- [75] S. Liu, S. Zhang, X. Li, S. Wang, C. Li, Synthesis and characterization of a new high near-infrared reflectance yellow pigment: $\text{Bi}_{2-x}\text{Er}_x\text{MoO}_6$, *Ceram. Int.* 49 (2023) 5456–5465, <https://doi.org/10.1016/j.ceramint.2022.10.069>.
- [76] L. Li, L. Feng, Y. Xiao, W. Xie, X. Sun, Synthesis and characterization of yellow pigments $(\text{Li}_{0.4}\text{RE}_{0.6}\text{Al}_{0.6})_1/2\text{MoO}_4\text{--BiVO}_4$ with high NIR reflectance, *ACS Sustainable Chem. Eng.* 9 (2021) 16606–16616, <https://doi.org/10.1021/acssuschemeng.1c05182>.
- [77] C. Ding, A. Han, M. Ye, Y. Zhang, L. Yao, J. Yang, Hydrothermal synthesis and characterization of novel yellow pigments based on V^{5+} doped BiPO_4 with high near-infrared reflectance, *RSC Adv.* 8 (2018) 19690–19700, <https://doi.org/10.1039/C8RA02406E>.
- [78] H.B. Frieboes, S. Raghavan, B. Godin, Modeling of nanotherapy response as a function of the tumor microenvironment: focus on liver metastasis, *Front. Biotechnol.* 8 (2020) 1011.
- [79] T.C.C. Lopez, I.M.A. Diniz, L.S. Ferreira, J. Marchi, R. Borges, S.P.H.M. de Cara, R. D'Almeida-Couto, M.M. Marques, Bioactive glass plus laser phototherapy as promise candidates for dentine hypersensitivity treatment, *J. Biomed. Mater. Res. Part B Appl. Biomater.* 105 (2017) 107–116, <https://doi.org/10.1002/jbm.b.33532>.
- [80] J. Stucke-Ring, J. Ronnacker, C. Brand, C. Hölte, C. Schliemann, T. Kessler, L. H. Schmidt, S. Harrach, V. Mantke, H. Hintelmann, W. Hartmann, E. Wardelmann, G. Lenz, B. Wunsch, C. Müller-Tidow, R.M. Mesters, C. Schwöppe, W.E. Berdel, Combinatorial effects of doxorubicin and retargeted tissue factor by intratumoral entrapment of doxorubicin and proapoptotic increase of tumor vascular infarction, *Oncotarget* 7 (2016) 82458–82472, <https://doi.org/10.18632/oncotarget.12559>.
- [81] T. Liang, G. Peng, X. Zhang, Y. Wei, X. Zheng, W. Luo, M. Dai, C. Deng, X. Zhang, Modulating visible-near-infrared reflectivity in ultrathin graphite by reversible Li-ion intercalation, *Opt. Mater.* 121 (2021) 111517, <https://doi.org/10.1016/j.optmat.2021.111517>.
- [82] X. Yan, T. Ohno, K. Nishijima, R. Abe, B. Ohtani, Is methylene blue an appropriate substrate for a photocatalytic activity test? A study with visible-light responsive titania, *Chem. Phys. Lett.* 429 (2006) 606–610, <https://doi.org/10.1016/j.cplett.2006.08.081>.
- [83] F. Parrino, V. Loddo, V. Augugliaro, G. Camera-Roda, G. Palmisano, L. Palmisano, S. Yurdakal, Heterogeneous photocatalysis: guidelines on experimental setup, catalyst characterization, interpretation, and assessment of reactivity, *Catal. Rev.* 61 (2) (2018) 163–213, <https://doi.org/10.1080/01614940.2018.1546445>.